A Comparative Electron Paramagnetic Resonance Study of the Nucleotide-Binding Domains' Catalytic Cycle in the Assembled Maltose ATP-Binding Cassette Importer

Mathias Grote,* Enrica Bordignon,† Yevhen Polyhach,‡ Gunnar Jeschke,‡ Heinz-Jürgen Steinhoff,† and Erwin Schneider*

*Institut für Biologie/Bakterienphysiologie, Humboldt Universität zu Berlin, Berlin, Germany; †Fachbereich Physik, Universität Osnabrück, Osnabrück, Germany; and ‡Fachbereich Chemie, Universität Konstanz, Konstanz, Germany

ABSTRACT We present a quantitative analysis of conformational changes of the nucleotide-binding subunits, $MalK_2$, of the maltose ATP-binding cassette importer $MalFGK_2$ during the transport cycle. Distance changes occurring between selected residues were monitored in the full transporter by site-directed spin-labeling electron paramagnetic resonance spectroscopy and site-directed chemical cross-linking. We considered S83C and A85C from the conserved Q-loop and V117C located on the outer surface of MalK. Additionally, two native cysteines (C350, C360) were included in the study. On ATP binding, small rearrangements between the native sites, and no distance changes between positions 117 were detected. In contrast, positions 85 come closer together in the ATP-bound state and in the vanadate-trapped intermediate and move back toward the apo-state after ATP hydrolysis. The distance between positions 83 is shown to slightly decrease on ATP binding, and to further decrease after ATP hydrolysis. Results from cross-linking experiments are in agreement with these findings. The data are compared with in silico spin-labeled x-ray structures from both isolated $MalK_2$ and the $MalFGK_2$-E complex. Our results are consistent with a slightly modified "tweezers-like" model of closure and reopening of $MalK_2$ during the catalytic cycle, and show an unforeseen potential interaction between MalK and the transmembrane subunit MalG.

INTRODUCTION

ATP-binding cassette (ABC) transporters are membrane proteins that mediate the uptake or export of an enormous variety of substrates at the expense of ATP. They are found in all organisms from bacteria to man and dysfunction is often associated with disease. ABC transporters share a common structural organization comprising two transmembrane domains (TMDs) that form the translocation pore and two nucleotide-binding domains (NBDs) that hydrolyze ATP (1). In fact, in most importers, that are confined to prokaryotes, TMDs and NBDs are expressed as separate protein subunits, whereas in most export systems of both prokaryotes and eukaryotes they are expressed either as half-transporters (fusion of one TMD to one NBD) or fused into a single polypeptide chain (2).

Recent times have seen a dramatic increase in knowledge on ABC transporter structures. The publication of x-ray diffraction data on whole transporters such as the multidrug-exporter Sav1866 (3), the vitamin B_{12}-importer $Btu(CD)_2$ with its substrate binding protein BtuF (4), the tungstate/molybdate importer-binding protein supercomplex $ModB_2C_2$-A (5), and the maltose importer supercomplex $MalFGK(E159Q)_2$-E (6) have provided a new framework for structural research on this class of membrane proteins. However, to obtain a deeper insight into how ABC transporters couple the chemical energy of ATP hydrolysis to conformational rearrangements that power substrate translocation, techniques analyzing the dynamics of these molecules in their active state have to be used. Among those, site-directed spin-labeling (SDSL) electron paramagnetic resonance spectroscopy (EPR) is an extremely powerful tool. This technique has the advantage that only the bound paramagnetic radicals are EPR active whereas the protein itself does not cause any background signal. Thus, assignment of signals to structural sites becomes trivial even in large and complex systems. Furthermore, unlike in NMR spectroscopy, it is possible to work with natural isotopes for protein preparation.

A spin label (SL) covalently attached to a cysteine residue of the protein allows to gain information on molecular surrounding, accessibility or motional constraints of the respective site in the protein (see Bordignon and Steinhoff for a recent review (7)). Having attached two spin labels to a protein, it is also possible to accurately determine distances between the nitroxide moieties due to the dipolar interactions between the magnetic moments giving rise to a dipolar broadening in the continuous wave spectra for distances in the 1–2 nm range or to a modulation of the intensity of the refocused echo in the 4-pulse double electron-electron resonance (DEER) experiments with accessible distances in the range 1.5–8 nm. The latter pulse sequence has already been successfully applied to membrane proteins such as the sodium/proline antiporter PutP of *Escherichia coli* (8), the bacterial lipid A-exporter MsbA (9), and the *E. coli* lactose permease (10).

Submitted February 28, 2008, and accepted for publication May 28, 2008.

Mathias Grote and Enrica Bordignon contributed equally to this work.

Address reprint requests to Enrica Bordignon, Tel.: 49-0541-9692664; Fax: 49-0541-9692656; E-mail: Enrica.Bordignon@uos.de.

Gunnar Jeschke's and Enrica Bordignon's present address is Laboratorium für Physikalische Chemie, ETH Zürich, 8093 Zürich, Switzerland.

Editor: Janos K. Lanyi.

0006-3495/08/09/2924/15 $2.00

doi: 10.1529/biophysj.108.132456

We now apply this method to the maltose ABC-importer of *E. coli*/*Salmonella typhimurium*. The maltose transporter consists of two transmembrane subunits, MalF and MalG, a homodimer of the nucleotide-binding subunits, $MalK_2$, at the cytoplasmic side of the membrane and the periplasmic maltose-binding protein, MalE (11,12). This transporter has served as a model for ABC import systems for more than two decades, leading to a plethora of genetic and biochemical data (11,12) that now can be interpreted in the light of the crystal structures of the isolated NBDs (13) and of the full transporter that has been solved for the ATP-bound state of the mutant $MalFGK(E159Q)_2$-E (6). The amino acid exchange in MalK abolishes ATPase activity and is thought to lock the complex in a transition state-like conformation (14). Furthermore, MalE is permanently bound to this mutant and hence could be co-crystallized.

Although MalF and MalG differ in the number of transmembrane segments (8 and 6, respectively) and their amino acid sequences, both contain the so-called ''EAA-motif'', also known as ''L-loop'' or ''coupling helix'', which are in contact with MalK (6). According to the crystal structure, MalF and MalG form a large central cavity for transport; however, maltose is only bound to MalF (6). The MalK subunits bind and hydrolyze ATP, thereby generating the power stroke necessary for the rearrangements of MalFG.

Like other nucleotide-binding domains from ABC transporters, MalK can be divided into a RecA-like subdomain comprising the Walker A- and B-motifs, that constitute the ATP binding site, and a specific α-helical subdomain encompassing the unique LSGGQ signature sequence (15). In addition, MalK contains a C-terminally located ''regulatory'' subdomain that forms a large part of the dimer contact surface. The catalytic cycle of the MalK dimer was postulated according to the crystal structures solved for isolated $MalK_2$ in the apo-state as well as for the ATP- and ADP-bound conformers (13). On binding of ATP, the α-helical and the RecA-like subdomains of MalK move into close proximity. Because the C-terminal domains do not show any significant motion, the closing of the MalK dimer has been metaphorically described as ''tweezers-like'' (16). After ATP hydrolysis has occurred, phosphate is released and the ADP-bound $MalK_2$ reopens to the semiopen form. Dissociation of ADP should then complete the catalytic cycle toward the open apo-state.

The α-helical and the RecA-like subdomains of MalK are connected by the Q-loop. This peptide region contains a conserved glutamine residue that binds to a Mg^{2+}-ion needed as cofactor. The x-ray structure of the fully assembled transporter shows that the Q-loops are in close proximity to the EAA-loops of MalFG and furthermore to a C-terminal tail of MalG protruding into the MalK-interface region (6). These structural findings are in line with a number of genetic and biochemical studies. By using site-directed cross-linking, Daus et al. (17) showed an asymmetric interaction of the Q-loops with MalF and MalG. Moreover, the open-to-close transition of $MalK_2$ on ATP binding and in the vanadate-trapped state was monitored via Q-loop residues. As can be seen from experiments using $MalK_2$ covalently locked in the closed state, flexibility of these regions is essential to complete the catalytic cycle of the transporter (17). Finally, a molecular dynamics simulation suggests that conformational switching of the Q-loops may mediate communication between TMDs and the catalytic sites (18).

In this study, we extend these studies on the Q-loop of MalK to a detailed analysis of distance changes carried out by continuous wave (cw) EPR and DEER spectroscopy. The distance constraints obtained at different stages of the transport cycle are compared with the crystal data of both isolated and assembled MalK domains to elucidate the mechanistic picture of the ATP-induced power stroke in the maltose ABC transporter. By spin-labeling the available crystal structures in silico and by simulating the interspin distances, a detailed comparison between the $MalK_2$ rearrangement in the isolated and assembled forms was obtained. We analyzed purified transport complex variants that contain cysteines replacing residues S83 and A85 from the Q-loop (Fig. 1), in the apo-, the ATP-bound, the vanadate-trapped, and the posthydrolysis state to monitor the closure and reopening of the MalK dimer during the transport cycle. Furthermore, we investigated the rearrangements of the outer surface of the MalK dimer by detecting the interspin distance between positions 117 in the two monomers (Fig. 1). Our results show that MalK-dimer closure and reopening in the assembled transporter is similar to the rearrangements derived from the structures of soluble $MalK_2$ at a quantitative level. However, our comparative approach also showed some important site-specific deviations. The open-to-close transition seems to imply larger movements in the isolated domains than in the assembled complex that might be due to the missing TMDs. Most notably, the C-terminal region of MalG seems to form potentially relevant interactions with the Q-loop region of MalK during the nucleotide-binding domains' catalytic cycle.

MATERIALS AND METHODS

Bacterial strains and plasmids

Plasmids were generally hosted in *E. coli* strain JM109. The *malK* alleles of *S. typhimurium* were subcloned into plasmid vector pSU19. Resulting plasmids pMM37 (His_6-MalK C40S), pMM40 (His_6-MalK C40S V117C) and pMG13 (His_6-MalK C40S A85C) are described in Daus et al. (17). The encoded MalK variants still contain native cysteines at positions 350 and 360 (C352 and C362 in *E. coli* MalK, respectively). For complex expression, plasmids harboring the respective *malK* alleles were combined with pMM34, carrying *malFG* alleles of *E. coli* that encode cysteine-free variants (17). The *mal* genes from both organisms are functionally fully exchangeable (19).

Construction of plasmids

Site-directed mutagenesis of *malK* was carried out using the Quik-change mutagenesis kit (Stratagene, La Jolla, CA). Plasmid pMM37 (17) served as template for the construction of pMG37 (His_6-MalK C40S S83C).

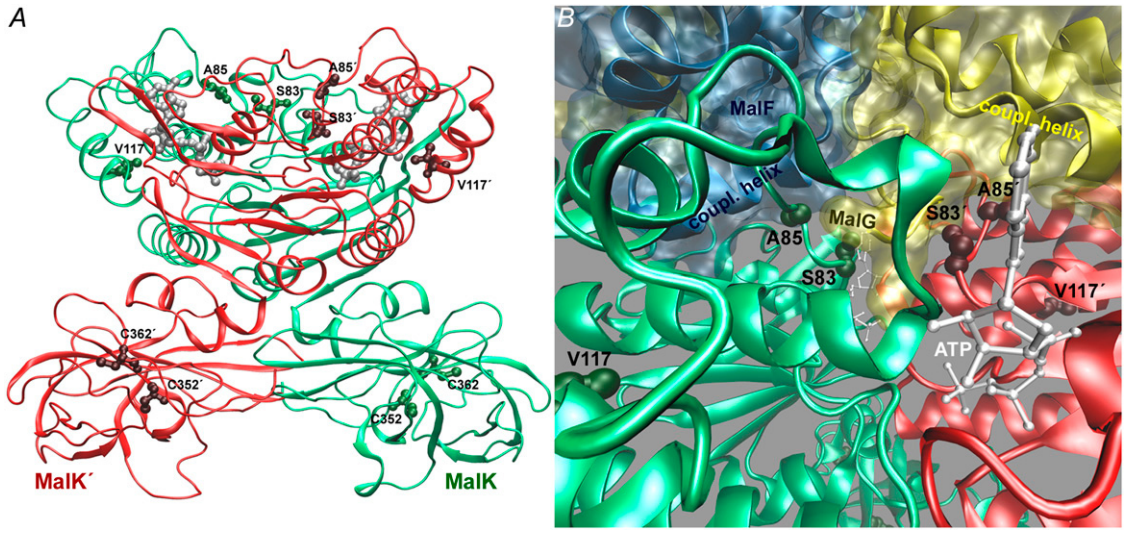

FIGURE 1 Ribbon diagram of the MalK subunits in the isolated and assembled forms. (*A*) Side view of the isolated $MalK_2$ domains in the ATP-bound form (*red* and *green ribbons*; PDB code 1Q1E) The residues engineered to cysteines in this study (S83, A85, and V117) and the residual native cysteines (positions 352 and 362 in *E. coli* MalK correspond to 350 and 360 in *S. typhimurium* MalK, respectively) present in the background construct MalF*G*$K(C40S)_2$ used for the investigation are represented in ball-and-stick models. The two ATP bound molecules are represented as ball-and-stick models in gray. (*B*) View on the Q-loops of the MalK domains (*red* and *green ribbons*) in the assembled complex (PDB code 2R6G). MalF and MalG are represented both as blue and yellow ribbons and as transparent surface models. The investigated residues and the ATP molecules bound to the supercomplex are represented as ball-and-stick models.

Purification of $MalFGK_2$ complexes

Polyhistidine-tagged complex variants were overproduced in strain JM109 harboring the respective plasmid combinations (see above). Purification was carried out as described in Landmesser et al. (20). However, in contrast to the published protocol, $MgCl_2$ was omitted from buffer 1 (to prevent hydrolysis in samples used for ATP-binding). Furthermore, complexes were eluted with 200 mM imidazole in buffer 1 instead of 50 mM as in Landmesser et al. (20).

Purification of MalE

Polyhistidine-tagged MalE was purified as described in Daus et al. (21).

Vanadate-trapping of $MalFGK_2$ complexes

The reaction mixture routinely contained a double molar excess of MalE over $MalFGK_2$. For cross-linking, 5 μM of MalE and 2.5 μM of $MalFGK_2$ were used. Furthermore, 0.01% maltose, 10 mM $MgCl_2$, 4 mM ATP, and 0.5 mM ortho-vanadate were added. The reaction was carried out in 50 mM Tris-HCl pH 8.0, 20% (v/v) glycerol, 0.01% β-dodecylmaltoside, for 30 min at 37°C. For spin-labeled samples the concentration of vanadate was reduced to 0.25 mM to prevent cross-reactions of SL with vanadate. However, efficiency of the trap as judged from the inhibition of ATPase activity (93%) was not affected significantly.

Spin-labeling of $MalFGK_2$ complexes

Generally, complexes carrying one engineered cysteine (at position 83, 85, or 117) in each MalK subdomain were incubated with threefold molar excess of the methanethiosulfonate spin label (MTSSL; Toronto Research Chemicals, Toronto, Canada) for 1 h at 4°C. These mild labeling conditions reduced the spin-labeling efficiency of the residual cysteines (C350 and C360). On the contrary, incubation with a 10-fold molar excess of MTSSL overnight at 4°C was used to maximize the labeling efficiency of C350 and C360 in MalF*G*$K(C40S)_2$. Residual MTSSL was removed by gel filtration (PD-10/NAP-columns; GE Healthcare, Freiburg, Germany). Samples were concentrated using Vivaspin 100 centrifuge filters (Sartorius, Goettingen, Germany) to a final concentration of 100–200 μM, flash frozen in liquid nitrogen and stored at −80°C until use. Spin labeling and EPR recordings were carried out in 50 mM Tris-HCl pH 8.0, 20% (v/v) glycerol, 0.01% β-dodecylmaltoside, except for MalF*G* $MalK(V117C)_2$ (asterisks denote cys-less variants) for which a buffer containing 20% (v/v) ^{2}D-glycerol was used to prolong the phase memory time.

ATP binding was achieved by incubating the spin-labeled samples with 4 mM ATP, 0.1 mM EDTA for 10 min at room temperature before shock freezing the sample in the quartz tube. After addition of 4 mM ATP, 4 mM $MgCl_2$, the sample was incubated for 30 min at 37°C before freezing.

Cross-linking with homobifunctional sulfonate cross-linkers

Sulfonate cross-linkers were purchased from Toronto Research Chemicals. The following cross-linkers were used: 1,2 ethanediylbismethanethiosulfonate (EBS); 1,6 hexandiylbismethane-thiosulfonate (HBS) and 3,6,9,12,15-pentaoxaheptadecan-1,17-diyl-bis-methanethiosulfonate (PBS). According to Loo and Clarke (22), the approximate spacer lengths are 0.52 nm (EBS), 1.04 nm (HBS), and 2.47 nm (PBS). Reactions were carried out as described in Daus et al. (17) using a protein concentration of 2.5 μM. Where indicated, complex variants were incubated with 2 mM ATP and 0.1 mM EDTA for 10 min at room temperature before the addition of cross-linkers. Vanadate-trapping was carried out as described above.

Continuous wave EPR experiments

EPR spectra for interspin distance determination were recorded at 160 K using a homemade EPR spectrometer equipped with a Bruker rectangular cavity. The magnetic field was measured with a B-NM 12 B-field meter (Bruker, Rheinstetten, Germany). A continuous flow cryostat Oxford ESR 900 allowed stabilization of the sample temperature to 160 K. The microwave power was set to 0.2 mW and the B-field modulation amplitude adjusted to 0.25 mT. Samples were loaded into EPR quartz capillaries (3 mm inner diameter, sample volume 40 μl).

Fitting of simulated continuous wave low temperature EPR spectra

Fitting of simulated dipolar broadened EPR powder spectra to the experimental ones detected at 160 K was carried out according to the method described in detail by Steinhoff et al. (23). Owing to the flexible spin-label side chain, a random distribution of nitroxide ring orientation with respect to the interspin distance vector is assumed. To account for a range of distances expected to arise from these different orientations, a Gaussian distribution of interspin distances is allowed. During the fitting procedure, the g-tensor values, two components of the A-tensor (A_{xx} and A_{yy}), and the line width parameters were fixed according to the values found from analysis of the respective labeled species in the absence of dipolar broadening. The parameters used are $g_{xx} = 2.0085$, $g_{yy} = 2.0061$, $g_{zz} = 2.0022$, $A_{xx} = 0.50$ mT, $A_{yy} = 0.50$ mT, and A_{zz} was variable to account for different polarity of the SL environment (24–26). To fit the dipolar broadened spectrum for the respective mutant in different conditions, the average interspin distance, the distance distribution width, and A_{zz} were allowed to vary.

Pulse EPR experiments

Dipolar time evolution data were obtained at X-band frequencies (9.3–9.4 GHz) with a Bruker Elexsys 580 spectrometer equipped with a Bruker Flexline split-ring resonator ER 4118X-MS3 and a continuous flow He cryostat (ESR900; Oxford Instruments, Oxfordshire, UK) controlled by an Oxford Instruments temperature controller ITC 503S. All measurements were carried out at 50 K using the four-pulse DEER experiment (27): $\pi/2(\nu_{obs}) - \tau_1 - \pi(\nu_{obs}) - t' - \pi(\nu_{pump}) - (\tau_1 + \tau_2 - t') - \pi(\nu_{obs}) - \tau_2 - echo$ (27). Time t' is varied, whereas τ_1 and τ_2 are kept constant, and the dipolar evolution time is given by $t = t' - \tau_1$. Data were analyzed only for $t > 0$. For the observer frequency pulses the $\langle x\rangle$ channels were used with pulse lengths of 16 ns for $\pi/2$ and 32 ns for π pulses. The electron electron double resonance π pulse length was set to 12 ns. A two-step phase cycling ($+\langle x\rangle, -\langle x\rangle$) is carried out on $\pi/2(\nu_{obs})$. The resonator was overcoupled to $Q \sim 100$; the pump frequency ν_{pump} was set to the center of the resonator dip and coincided with the maximum of the nitroxide EPR spectrum, whereas the observer frequency ν_{obs} was 65 MHz higher and coincided with the low field local maximum of the spectrum. Proton modulation was averaged by adding traces at eight different τ_1 values, starting at $\tau_{1,0} = 200$ ns and incrementing by $\Delta\tau_1 = 8$ ns. In the presence of deuterated glycerol used for its effect on the spin-lattice relaxation, deuterium modulation was averaged by adding traces at eight different τ_1 values, starting at $\tau_{1,0} = 400$ ns and incrementing by $\Delta\tau_1 = 56$ ns. The total measurement time for each sample was between 6 and 14 h. The data analysis of the DEER traces was carried out with the software DeerAnalysis 2006.1 (28).

Simulation of distance distributions

Simulated distance distributions were constructed according to the approach based on a rotamer library of spin-labeled residues described in detail in Jeschke and Polyhach (29). A new rotamer library consisting of 98 rotamers of MTSSL attached to cysteine was used that was derived by geometry optimization of the 108 expected rotamers with a density functional theory approach. Ten rotamers were rejected subsequently due to internal clashes. Neglecting internal rotamer energies, populations for individual rotamers were calculated at 175 K that is our estimate for the glass transition for the water-glycerol mixture. It was checked that a choice of other temperatures does not lead to strong changes as long as the temperature is above 150 K. These populations were used as weights in the simulation of distance distributions. To account for additional broadening due to vibration of the label the distance distribution was convoluted with a Gaussian broadening function with a width of 0.1 nm. A more detailed discussion on using rotamer libraries in the structure determination of proteins will be published elsewhere (Ye. Polyhach, D. Hilger, H. Jung, and G. Jeschke, unpublished). Crystal structures used were nucleotide-free MalK (Protein Data Bank (PDB)-accession number 1Q1E (16)), ATP-bound MalK (1Q12 (16)), ADP-bound MalK (2AWN (13)), and the ATP-bound form of $MalFGK_2$-E E159Q (2R6G (6)).

Analytical procedures

Hydrolysis of ATP was assayed in microtiter plates essentially as described in Landmesser et al. (20). Protein concentrations were determined by the method of Dulley and Grieve (30). SDS-polyacrylamide gel electrophoresis was carried out with 10% polyacrylamide gels as described in Landmesser et al. (20).

RESULTS

Establishing an experimental system for EPR-analyses of the maltose transporter

EPR measurements were carried out on purified detergent-solubilized MalF*G*K(C40S)$_2$ complex variants (asterisks denote cys-less variants of MalF and MalG) spin-labeled at positions 83, 85, and 117 in the MalK subunits, respectively. ATPase-activity was assayed routinely for each mutant before and after spin-labeling. Activities for all three cysteine variants ranged from 0.6 to 0.8 μmol phosphate $\times$ min^{-1} $\times$ mg^{-1} protein and thus were $\sim$2 to 2.5 times higher than found recently for MalF*G*K (C40S)$_2$ (17). Possibly, this might be due to the modified purification protocol as described under Materials and Methods. Spin-labeling did not significantly affect the enzymatic activities of MalF*G*K(C40S)$_2$ and MalF*G*K(C40S V117C)$_2$ (90% residual activity). In contrast, labeling of positions 83 or 85 caused a drop in ATPase activity to 50% and 20%, respectively, as compared with the unlabeled control.

Native cysteines: test experiments and data evaluation

We carried out control experiments to prove the suitability for EPR analysis of the MalF*G* K(C40S)$_2$ complex carrying two residual native cysteines in the C-terminal domain of each MalK subunit (C350, C360, see Fig. 1). Both residues, when mutated to either serine or alanine caused a dramatic loss in the stability of the protein (data not shown). Although C350 and C360 have been shown previously to be only poorly accessible to thiol reactive compounds, including spin-labels (17), a thorough investigation appeared appropriate. First, the eventual presence of detectable interspin distances was investigated by pulse EPR (DEER) on the MalF*G*K(C40S)$_2$ complex. Second, a labeled cysteine variant, MalF*(T92R1) G*K(C40S)$_2$, (in the following, R1 denotes the MTSSL side chain) was investigated by DEER to quantify possible effects of labeled residual cysteines on the background decay function and, consequently, on the fit to obtain the distances in the engineered doubly labeled mutants. The use of a spin-labeled position in MalF rather than in MalK to test for residual spin-labeling of the native cysteines is based on the rationale

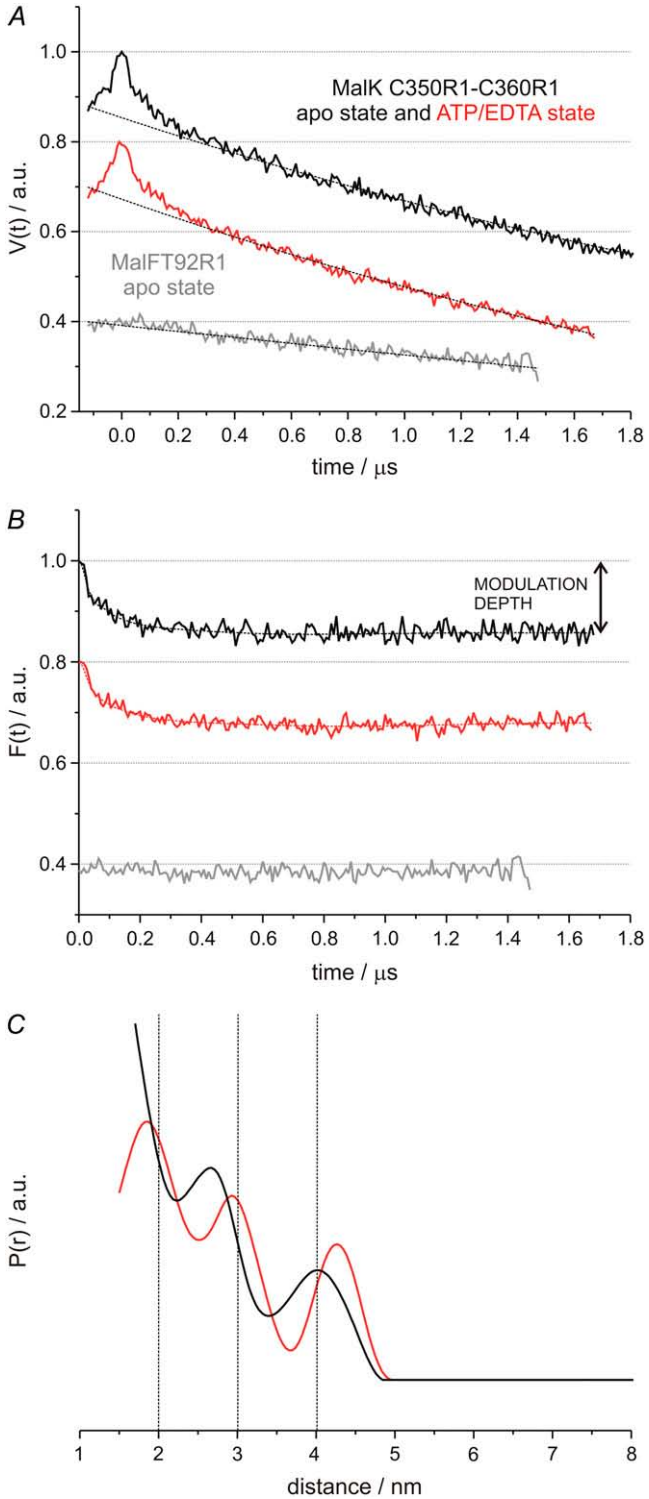

FIGURE 2 DEER measurements on the background construct MalF* G*K(C40S)$_2$ in the absence (*apo, black*) and presence (*red*) of ATP/EDTA and on the mutant MalF*(T92C)G*K(C40S)$_2$ in the absence of ATP (*gray*). The spectra are described in the figure only by the subunit carrying the cysteine/s and the respective residue number (R1 denotes the MTS spin label residue). (*A*) Experimental data $V(t)$ (colored according to the legend) and exponentially decaying background arising from a three-dimensional distribution of remote spins (*black dashed lines*), as fitted by DeerAnalysis 2006.1 (28). (*B*) Background corrected experimental data $F(t)$ and fit by the Tikhonov regularization with a regularization parameter $\alpha = 100$ (*dashed lines*). (*C*) Distance distribution $P(r)$ for the MalK C350R1-C360R1 in the two states (colored according to the legend).

that MalF is present as a single copy in the transporter. Thus, no interspin distances are expected to arise from the singly labeled mutant chosen. The upper two traces in Fig. 2 *A* represent the dipolar evolution function ($V(t)$) for MalF*G*K(C40S)$_2$ labeled with a 10-fold molar excess of MTSSL overnight at 4°C. Traces were obtained in the absence (apo-transporter) and in the presence of ATP/EDTA. The third trace in Fig. 2 *A* was obtained with MalF*(T92R1)G*K(C40S)$_2$ labeled with a threefold molar excess of MTSSL for 1 h at 4°C (i.e., milder labeling conditions). Superimposed to the traces, the background fit with an exponential function ($B(t)$) due to a homogeneous three-dimensional distribution of the spins in the sample is presented. It is immediately clear from the inspection of the two upper traces that a slow oscillation dampening within the first microsecond is present, indicating the presence of dipolar interactions. On the contrary, such oscillations are absent in the third trace that can be simply fitted with the exponential background decay function.

The results point to two facts: first, interspin distances can be detected in the MalF*G*K(C40S)$_2$ construct indicating a small but detectable spin-labeling of the native residual cysteines; second, the reaction between MTSSL and the residual native cysteines is strongly suppressed under mild reaction conditions that nevertheless lead to efficient spin-labeling of highly accessible cysteines (as in the case of MalF*(T92C)), hence no interspin distances are detectable due to the labeled residual cysteines. Thus, we conclude that our variants of the transporter are suited for the intended study.

Fig. 2 *B* represents the form factors, $F(t)$, obtained by dividing $V(t)$ by $B(t)$ and renormalizing at zero time and the fits obtained by the Tikhonov regularization with an α parameter 100. The small modulation depth obtained (15%, ~1 spin in average per complex) indicates clearly the poor accessibility of the native cysteines toward MTSSL (31,32). In Fig. 2 *C*, the distance distribution P(r) for MalK (C350R1-C360R1) in the two states is presented. Due to the poor signal/noise ratio and to the insufficiently long time traces for the accurate extraction of the distance distributions, the data analysis is affected by large uncertainties. Thus, an interpretation of the distance distribution must be carried out with care. The obtained broad distance distribution may be interpreted in terms of three main interspin distance peaks, one of which characterized by distances <2.0 nm. Indication for a slight shift toward longer distances in the overall distance distribution is found on ATP binding. The results are in line with the Cβ-Cβ distances determined from the x-ray structures of isolated *E. coli* MalK$_2$ (see Table 1). In fact, in the apo-state a short intraMalK Cβ-Cβ distance between positions 352 and 362 (1.1 nm) is expected (positions 352 and 362 in *E. coli* MalK correspond

TABLE 1 Experimental EPR data compared with simulated interspin distances and Cβ-Cβ distances from crystal structures of MalK subunits both isolated (apo-, ATP-, and ADP-bound states) and assembled in the transporter (ATP-bound state)

	Experimental interspin distances		Simulated interspin distances		X-ray structure
	Mean distance (nm)	Distance distribution (FWHM) (nm)	Mean distance (nm)	Distance distribution (FWHM) (nm)	Cβ-Cβ distance (nm)
MalF*G*K(C40S)$_2$					
Apo-state	**<2–5***	**n.d.**	n.a.	n.a.	1.1/3.8/4.7/5.6[†]
ATP-bound state	**<2–5***	**n.d.**	n.a.	n.a.	1.2/3.8/4.8/5.8 **1.0/3.9/4.7/5.5**
MalK 83					
Apo-state	**2.00**	**0.9**	2.8	1.0	2.9
ATP-bound state	**1.75**	**1.0**	1.4/**1.8**	0.8/**0.5**	0.9/**0.9**
Posthydrolysis state	**1.5**[‡]	**0.7**[‡]	1.5	1.2	1.6
Vanadate-trapped state	**1.6**[‡]	**0.8**[‡]	n.a.	n.a.	n.a.
MalK 85					
Apo-state	**2.8**[§]	**2**	3.1	1.0	3.4
ATP-bound state	**1.85 (1.8**[‡]**)**	**1.5 (1.4**[‡]**)**	2.1/**1.9**	1.1/**0.7**	1.9/**1.7**
Posthydrolysis state	**1.95/3.0**	**3**[¶]	2.5	1.2	2.6
Vanadate-trapped state	**1.5/2.9 (1.7**[‡]**)**	**1**[§] **(0.8**[‡]**)**	n.a.	n.a.	n.a.
MalK 117					
Apo-state	**6.0**	**1.0**	7.0[‖]	n.a.	6.0
ATP-bound state	**6.0**	**0.9**	5.2[‖]/**5.2**[‖]	n.a.	4.3/**4.2**

Abbreviations: FWHM, full width at half-maximum; n.a., not available; n.d., not determined.

*Experimental and simulated values obtained from MalK assembled in the supercomplex (PDB code 2R6G) are depicted in bold. In the presence of multiple distance peaks or large distances (5–6 nm), the estimated error due to background subtraction is $\pm$0.5 nm; for the other cases the estimated error is $\pm$0.05 nm. In the case of the construct MalF*G*K(C40S)$_2$, the broad distance distribution detected does not allow a precise assignment of the mean distances.

[†]Cβ-Cβ distances for the background construct are presented for C350–C360, C350–C350′, C350–C360′, and C360–C360′, respectively, with the prime indicating the side chain in the opposing monomer.

[‡]Mean distance and FWHM obtained from the fit with the program ''dipfit'' of simulated spectra to the continuous wave EPR spectra recorded at 160 K. Error estimated to be $\pm$0.1 nm.

[§]Due to the relative short time range available for the dipolar evolution for the MalK85 samples, the accuracy in the determination of the distance peaks at ~4–5 nm is poor, thus they are not listed in the table.

[¶]Estimated FWHM value for the short distance peak.

[‖]Indicative values of the interspin distances obtained from internitrogen distances of in silico spin-labeled positions in the isolated MalK$_2$ domains in the absence and presence of ATP (PDB codes 1Q1E and 1Q12) and in the assembled complex (PDB code 2R6G). A pair of label rotamers was arbitrarily chosen where the dihedral angles of the nitroxide moieties were allowed to move until a position free from steric constraints was found.

to 350 and 360 in *S. typhimurium* MalK, respectively), which is changed only slightly in the ATP-bound state (1.2 nm in the isolated domains and 1.0 nm in the complex). The distances observed in the range <2 nm in the apo- and ATP-bound states are tentatively assigned to this interaction. The Cβ-Cβ interMalK distance between 352 and 352′ is 3.8 nm for both apo- and ATP-bound x-ray structures of the isolated domains (3.9 nm in the complex), in line with the 2.7/3.0 nm interspin distance peaks detected by DEER in the two states. The additional long distance value detected by DEER at ~4 nm is assigned to the interaction between 352 and 362′. The interMalK distance between positions 362–362′ is expected to be in the range of 6 nm, beyond the DEER range for the dipolar evolution time chosen for the measurements.

Outer surfaces of MalK$_2$: no distance changes detected

Fig. 3 shows the DEER analysis carried out on the MalF*G*K(C40S, V117R1)$_2$ mutant in the apo- and ATP-bound state. These positions were chosen due to their location on the outer surfaces of the NBDs (16). To maximize the dipolar evolution time, thus allowing a more reliable fit for the long interspin distances expected, deuterated glycerol was added to the buffer. The dipolar evolution time could be prolonged to 2.8 and 3.2 μs in the apo- and ATP/EDTA-bound states, respectively, which is sufficient to detect one dipolar oscillation due to a 4–6 nm interspin distance, but still too short to have a reliable fit of the background function $B(t)$. In fact, to obtain a reliable separation of a dipolar evolution function $V(t)$ into form factor $F(t)$ and background factor $B(t)$ the DEER trace should be observed up to a time at which the dipolar oscillation has completely decayed. The position and width of the distance peak can be hence affected by a large error. The small modulation depth detected (20%) indicates a relatively low spin-labeling efficiency for these positions (1.4 spins calculated per complex) that are characterized by an interspin distance centered at ~6 nm both in the apo- and ATP-bound states. The data show that the distance between the outer surfaces of the MalK dimer in the assembled complex are not changed on ATP binding. No relevant peaks due to the presence of spin-labeled native cysteines were present, again

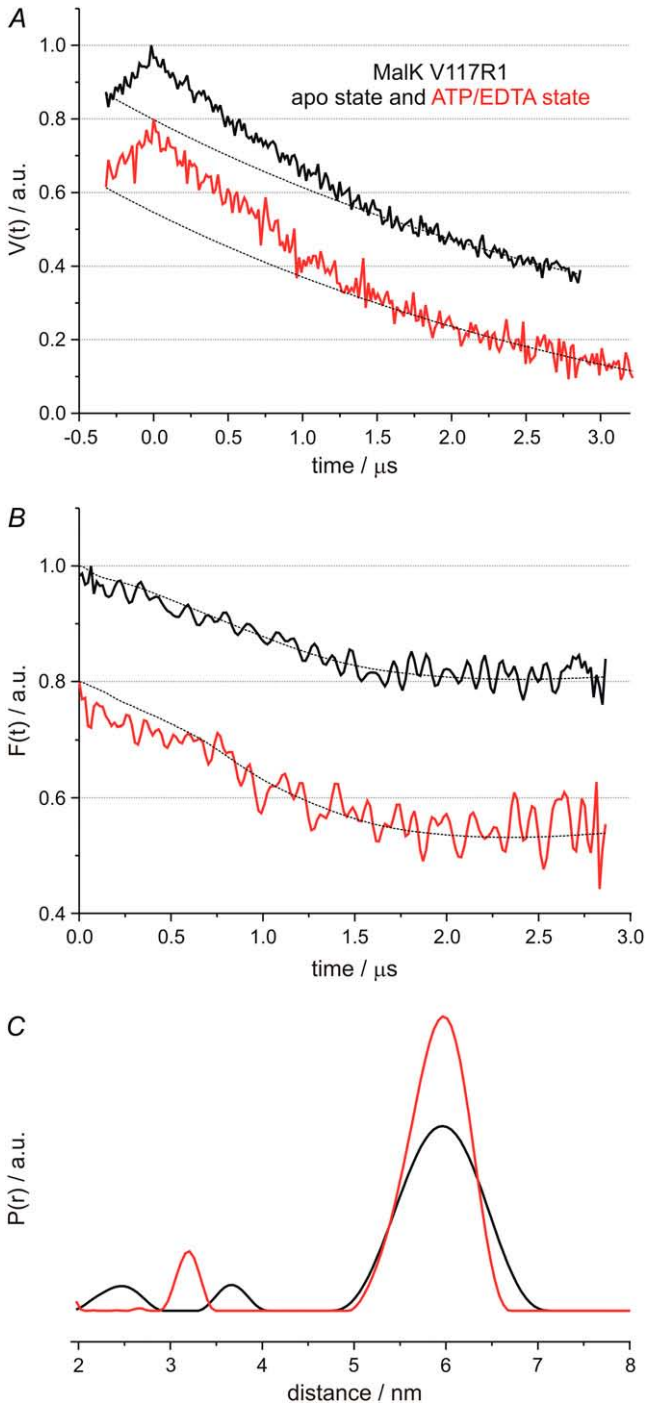

FIGURE 3 DEER measurements on the MalF*G*K(C40S, V117C)$_2$ spin-labeled mutant in the absence of ATP (*apo, black*) and in the presence of ATP/EDTA (*red*). Details according to Fig. 2.

confirming our previous conclusions. To address the effect of the spin-label side chain conformation on the interspin distances obtained experimentally, the MTS spin-labels were attached in silico to positions 117 and the *N-N* distance was determined for an arbitrarily chosen couple of rotamers. The dihedral angles of the nitroxide moieties were allowed to move until a position free from steric constraints was found (Table 1). A relatively large decrease in interspin distance was obtained in the isolated domains going from the apo- to the ATP-bound state (7.0 –5.2 nm) for the chosen couple of rotamers. Interestingly, the assembled complex shows an interspin distance close to 5 nm, in line with the experimental data. The closure of the N-terminal domain of the NBDs in the complex shows striking differences with respect to the isolated subunits.

Distance changes in the Q-loop region show closure and reopening of the MalK dimer

The DEER analysis carried out on the MalF*G*K(C40S, A85R1)$_2$ variant is shown in Fig. 4. The experiments were carried out for four different states of the transporter: the ATP-free (apo-state), the ATP/EDTA-, the posthydrolysis- and the vanadate-trapped state. As suggested by ATPase measurements of the spin-labeled protein, position 85 in MalK seems to be particularly sensitive toward chemical modifications (see above). Thus, one might expect that spin-labeling will also influence the conformational stability of its neighboring region. A broad distance distribution is found between the two MalK(C40S, A85R1) subunits (Fig. 4 *B*) for all states investigated. The absence of a unique well-defined distance might be related to the disturbing effect of spin-labeling on the overall structural stability at this position (see for comparison Fig. 5 *B* showing the narrower distance distribution between positions 83, located only two residues apart). Room temperature EPR spectra of position 85 also showed a multicomponent behavior, in line with this suggestion. No evidence for completely unfolded MalK subunits was found. Those peaks that are insensitive to the addition of cofactors are most probably due to inactive complexes and thus will not be analyzed. We thus concentrate on the most prominent peaks and observe their shifts for different states of the transporter. The most prominent peak in the apo-state is centered at 2.8 nm (Fig. 4 *B*). In the ATP-bound state, a decrease in the modulation depth and a drastic shift of the distance distribution with a main distance peak centered at 1.85 nm are observed. This relatively short distance is borderline between pulse and cw-EPR analysis. A low temperature cw-EPR spectrum was recorded on the same sample and a lineshape analysis was carried out with the program ''dipfit''. Comparison with the spectrum of the apo-state of the protein where short distances are absent showed an interspin distance of 1.8 nm with an estimated error of $\pm$0.1 nm. The distance distribution panels of Fig. 4 *B* show excellent agreement of the distances obtained by cw and pulse EPR. The results show the complementary character of the two techniques for distances in the 1–2 nm range. The 1-nm interspin distance decrease on ATP binding is clear evidence for $MalK_2$ closure. Interestingly, no spectral changes are observed in the room temperature cw EPR spectra, indicating that even a significant change in interspin distance is not always accompanied by visible changes in the spin label dy-

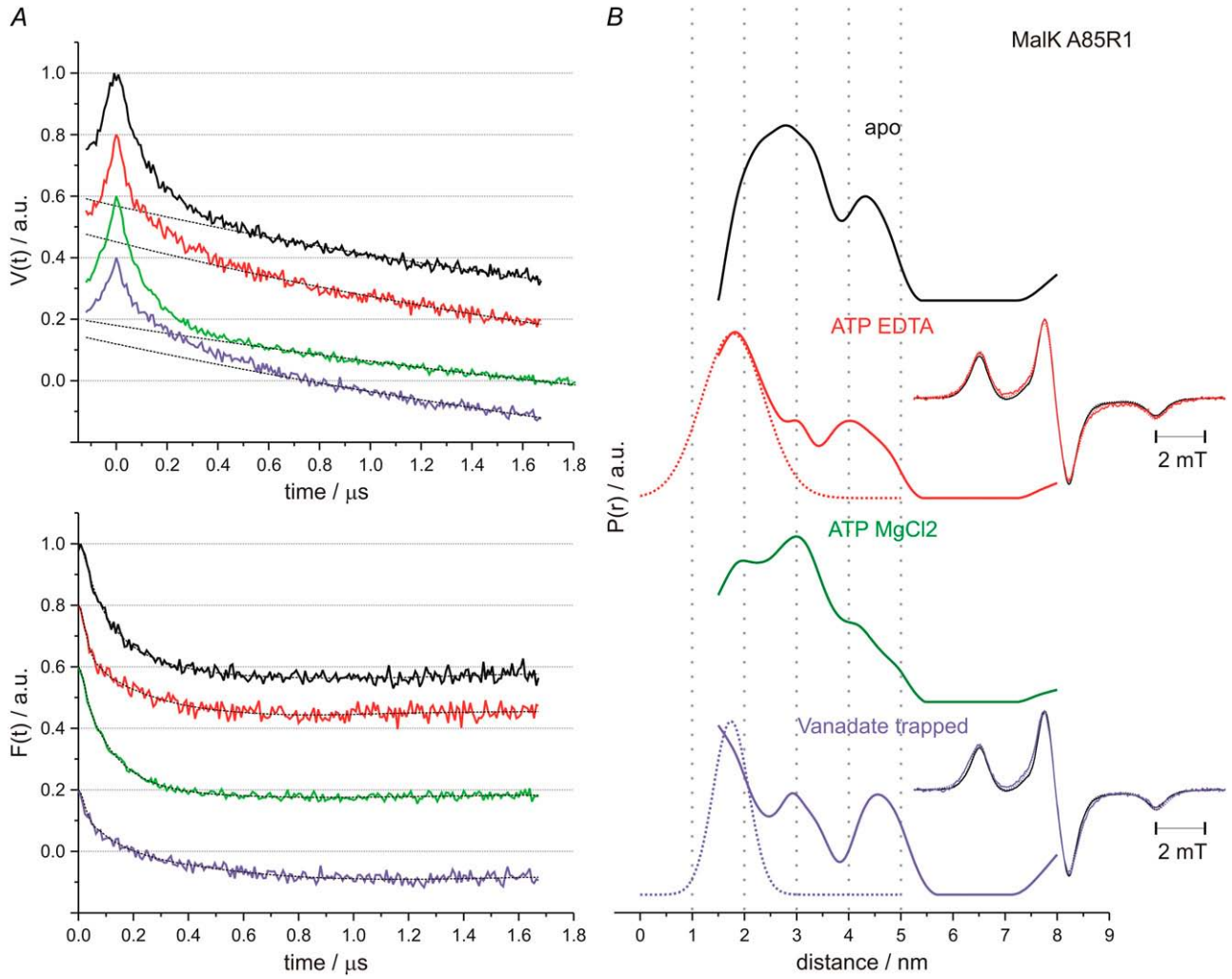

FIGURE 4 DEER measurements on the MalF*G*K(C40S, A85C)$_2$ labeled mutant in the absence of ATP (*apo*, *black*), in the presence of ATP/EDTA (*red*), in the posthydrolysis state (*green*) and in the vanadate-trapped state (*violet*). (*A*) Upper panel, experimental data $V(t)$ (colored according to the legend) and exponentially decaying background arising from a three-dimensional distribution of remote spins (*dashed lines*), as fitted by DeerAnalysis 2006.1 (28); bottom panel, background corrected experimental data $F(t)$ and fit by the Tikhonov regularization with a regularization parameter $\alpha = 1000$ (*dashed lines*). (*B*) distance distribution $P(r)$ for the different states obtained by the fit (colored according to the legend). For specific cases, additional low temperature cw measurements were carried out to obtain precise information on the distance <2 nm (*dotted lines*). The cw spectra are presented in the insets (colored according to the legend). The peak distances and line widths obtained are listed in Table 1.

namics (data not shown). Indeed such behavior is expected unless the two moieties approach so closely that spin label dynamics are restricted by collisions with neighboring side chain or backbone atoms.

In the posthydrolysis state, a broad distribution of distances is restored, which does not enable a clear assignment of peak distances. Two main peaks are present, one at 1.95 nm and the second at ~3.0 nm. Both peaks indicate a reopening of the MalK dimer after ATP hydrolysis, in agreement with cross-linking data published previously (17). The DEER analysis of the vanadate-trapped state indicates a broad distance distribution, with two peaks at 2.9 and 4.5 nm and an indication for distances <1.5 nm. The stronger suppression of the dipolar modulation depth (31) in the vanadate-trapped state with respect to the ATP-bound state (Fig. 4 *A*, *bottom panel*) indicates that a significant population of the transporter is responsible for the observed short distance. By cw-EPR lineshape analysis an interspin distance of 1.7 ± 0.1 nm with a very narrow distance distribution is found. Thus, we assign this to the interspin distance in the transition state. The results for positions 85–85′ are in line with a closure of the MalK subunits on ATP binding, a transition state characterized by similar short distances, and a reopening of the dimer toward an apo-state-like conformation after completion of hydrolysis.

In contrast to the data obtained for MalF*G*K(C40S, A85R1)$_2$ (Fig. 4), the DEER data obtained for MalF*G*K(C40S, S83R1)$_2$ (Fig. 5) in the apo-state show clearly a well-defined interMalK distance of 2.0 nm with a narrow distance distribution characterized by full width at half-maximum of 0.9 nm (Table 1). These results suggest a spin-label side chain

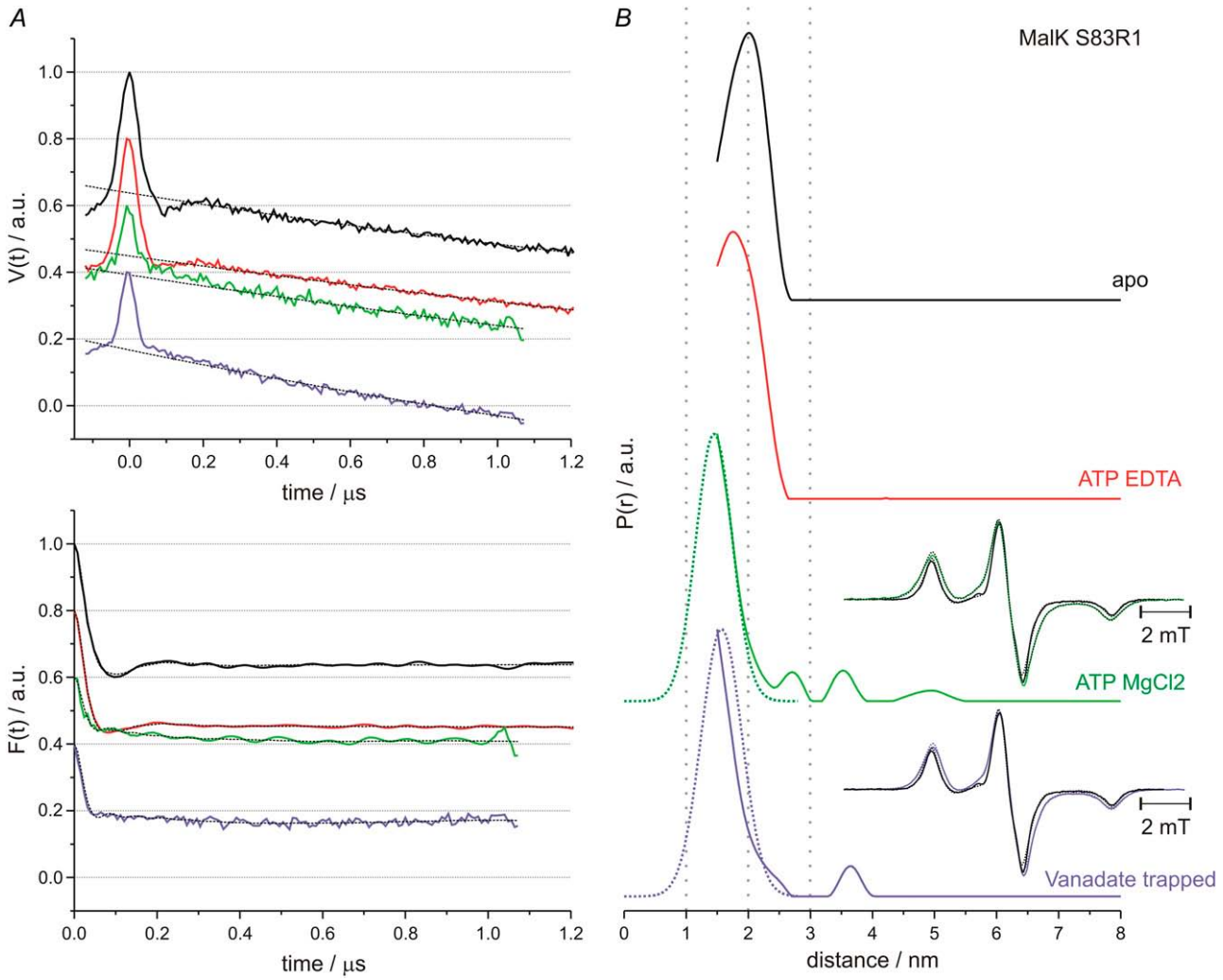

FIGURE 5 DEER measurements on the MalF*G*K(C40S, S83C)$_2$ labeled mutant in the absence of ATP (*apo*, *black*), in the presence of ATP/EDTA (*red*), in the posthydrolysis state (*green*), and in the vanadate-trapped state (*violet*). Details according to Fig. 4, except for a Tikhonov regularization parameter $\alpha = 100$ used for the fit.

with limited reorientational freedom due to secondary and tertiary interactions within the protein. EPR room temperature cw-spectra detected for position 83 indeed show a powder-like spectrum suggesting that the label is already motionally restricted (data not shown).

In the ATP-bound state, the interMalK S83R1 distance is decreased to 1.8 nm, indicating a closure of the nucleotide-binding domains, although to a smaller extent than what was observed for position 85. The narrow distance distribution and the good signal/noise ratio of the DEER trace allows to define this 0.2 nm distance change as significant. After ATP hydrolysis in the presence of $MgCl_2$, the modulation depth of the obtained form factor $F(t)$ function is reduced by almost 50% (Fig. 5 *A*, *bottom panel*) indicating the presence of interspin distances <1.5 nm (31). This is in agreement with the shape of the distance distribution function (Fig. 5 *B*) that points clearly to the presence of short distances. Analysis of the cw EPR spectrum leads to the determination of an interspin distance of 1.5 ± 0.1 nm in the posthydrolysis state. Agreement between the distance distribution obtained by DEER (*straight line*) and the cw-obtained Gaussian distance distribution (*dotted line*) is shown clearly in Fig. 5 *B*. For the vanadate-trapped conformer, which mimics the transition state during ATP hydrolysis, the distance determined by cw-EPR is 1.6 nm, close to the posthydrolysis state distance.

The results for positions 83–83′ are in line with a slight approach of these residues on ATP binding, a transition state characterized by even shorter distances, and a posthydrolysis state that does not show a reopening of the structure to the apo-state, but resembles the vanadate-trapped state.

Site-directed cross-linking of MalF*G* K(C40S, S83C)$_2$ with sulfonate cross-linkers

To estimate interMalK distances by an independent method, we additionally carried out chemical cross-linking experi-

ments with MalF*G*K(C40S, S83C). The expected distance changes should be in a detectable range for this approach. This strategy allows to complement the EPR data, but also to identify possible artifacts due to steric constraints of the nitroxide rings and protein side chains. Furthermore, these experiments permit us to compare the cross-linking patterns of this residue in the Q-loop to those published in an earlier study for the nearby residue A85 (17).

Chemical cross-linking with sulfonate reagents was carried out as described in Materials and Methods. Fig. 6 *A* shows a Coomassie-stained SDS-gel obtained for MalF*G*K(C40S, $S83C)_2$ in three conformational states that were also analyzed in DEER-experiments (apo-, ATP-bound-, and vanadate-trapped states). In the apo-state, substantial amounts of cross-link product, identified by immunoblotting as K-K dimer, were formed with HBS (1.0 nm) and PBS (2.5 nm) only. In contrast, in the ATP-bound state, the shortest linker (EBS, 0.5 nm) also produced significant amounts of K_2. This is consistent with a tweezers-like closure of the MalK-dimer on substrate binding. In the vanadate-trapped state, almost equal amounts of cross-link product were observed for all three sulfonates.

These results corroborated the EPR findings on S83R1 that also point to an ATP-dependent closure of the MalK-dimer, which thus would be in its tightest conformer after vanadate-trapping. The fact that changes in the cross-linking pattern on ATP addition are in agreement with the EPR data and are not as pronounced as one would expect from the predicted distance shift from 2.9 to 0.9 nm in the crystal structures of isolated $MalK_2$ (the most prominent K-K-dimer band should then be formed by HBS) suggests that, most likely, the Q-loop rearrangement is different in the complex-assembled and in soluble MalK. The open-to-close transition implies larger movements in the latter that might be due to the missing TMDs.

In Fig. 6 *B*, the same kind of analysis is shown for MalF*G*K(C40S, $A85C)_2$, carried out previously (17). When comparing these data to those for S83C, the overall pattern looks very similar; however, there are subtle differences. In the apo-state, A85C does form substantial amounts of a K-K-dimer with PBS (2.5 nm) only, whereas S83C shows a significant reaction product also with HBS (1.0 nm). This again corresponds nicely with larger interspin distances detected by EPR for A85 than for S83 in the apo-states (Table 1).

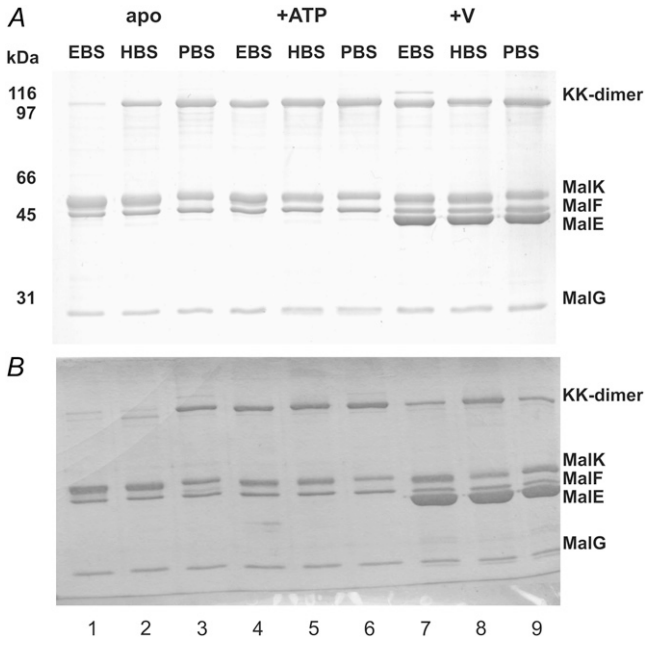

FIGURE 6 Chemical cross-linking of purified complex variants in detergent solution. Purified complex mutants were incubated in buffer alone (*apo, lanes 1–3*), with ATP/EDTA (*+ATP, lanes 4–6*), and after vanadate-trapping (*+V, lanes 7–9*) before cross-linking with homobifunctional sulfonate cross-linkers EBS (0.5 nm), HBS (1.0 nm), and PBS (2.5 nm; see Materials and Methods for details). Ten microliters of the cross-linking reaction mixture were loaded on a 10% SDS-gel and proteins were separated under nonreducing conditions. (*A*) MalF*G*K(C40S, $S83C)_2$. (*B*) MalF*G*K(C40S, $A85C)_2$ (see also (17)).

Interspin distance simulation based on a rotamer library approach

To improve reliability in the comparison between the EPR data obtained from spin-labeled complexes and the x-ray structures, in silico spin-labeling of positions 83 and 85 (Fig. 7) was carried out in all available structures and simulation of the expected interspin distances was obtained based on a rotamer library approach (see Materials and Methods). Results of the simulations for positions 83 and 85 are presented in Fig. 8 (all simulated values are listed in Table 1), superimposed to the experimentally determined interspin distance distributions and the cross-linking data.

The simulated interspin distances in the isolated structures follow the tweezers-like trend suggested for the native side chains. In fact, the distance between the two selected positions first decreases on ATP binding and then slightly increases again in the posthydrolysis state. This trend of distance changes is more evident for the label attached to position 85. Simulations in the MalK subunits assembled in the complex differed only slightly from the ATP-bound state of the isolated subdomains. This corroborates the finding that the structure of MalK in the complex is essentially identical to that of the isolated MalK dimer (6).

The simulations carried out in the subunits assembled in the complex are in excellent agreement with the experimentally determined distances in the ATP-bound state of the detergent-solubilized complexes. In the apo- and posthydrolysis-states deviations are observed between the experimental data and the interspin distances simulated for the isolated structures. This suggests that the Q-loop region is affected by the transmembrane subdomains, in particular at position 83. The important deviations between the tweezers-like motion suggested from x-ray crystallography in the isolated subunits and the opening and closure in the complexes will be addressed further in the following section.

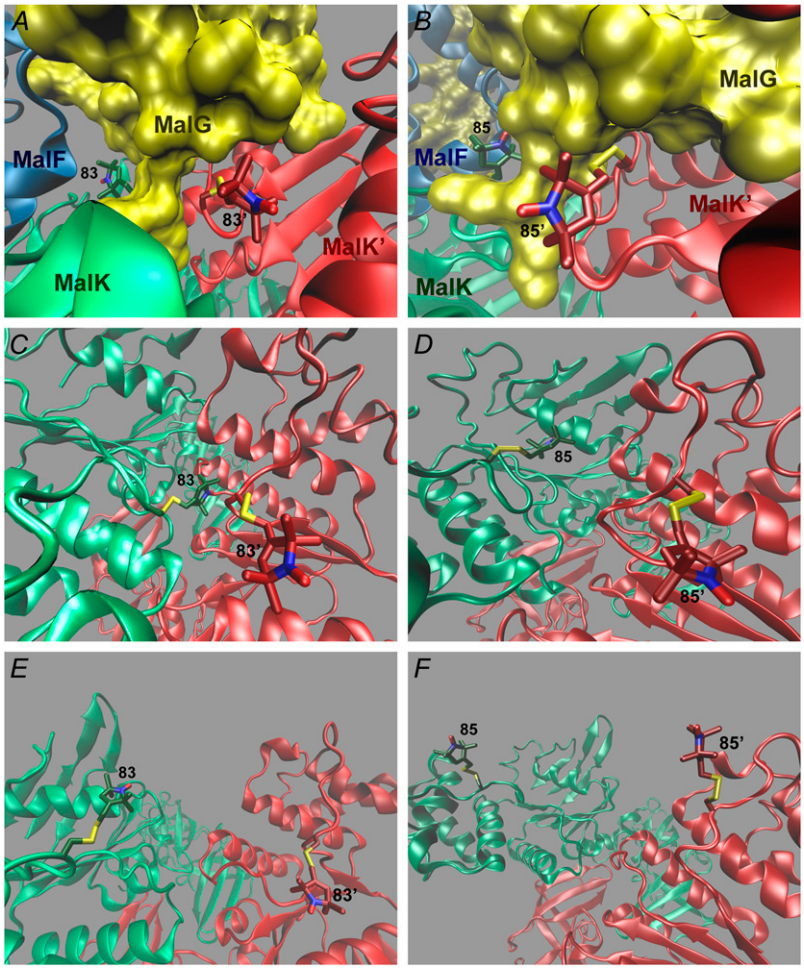

FIGURE 7 Spin labels attached at positions 83 and 85 of $MalK_2$ both in assembled and isolated forms. (*A* and *B*) View on the Q-loops of the MalK domains (*red and green ribbons*) in the assembled complex (2R6G). MalF is represented as blue ribbons and MalG as surface model. Two arbitrarily selected rotamers are represented as ball-and-stick models, with the nitrogen atoms highlighted in blue (N-N distances 2.0 and 1.2 nm, for 83-83′ and 85-85′, respectively). The ATP molecules were omitted for sake of clarity. (*C* and *D*) View on the Q-loops of the MalK domains (*red and green ribbons*) in the isolated $MalK_2$ in the ATP-bound form (1Q1E). Two arbitrarily selected rotamers are represented as ball-and-stick models (N-N distances 1.6 and 2.2 nm, for 83-83′ and 85-85′, respectively). (*E* and *F*) View on the Q-loops of the MalK domains (*red* and *green ribbons*) in the isolated $MalK_2$ in the apo-state. Due to the lack of steric constraints in the open state, several rotamers of the spin labels are equally energetically favored; two rotamers arbitrarily chosen among the several possible are presented (N-N distances 2.9 and 3.4 nm, for 83-83′ and 85-85′, respectively).

DISCUSSION

Models for coupling the catalytic cycle of NBD to substrate translocation have been proposed on the basis of the recently published structures of ABC-importers (6,33). Liganded substrate binding protein would bind to a transporter whose TMDs are open to the cytoplasm (inward-facing conformation), as found for example for the structure of the nucleotide-free form of the molybdate-tungstate importer $ModB_2C_2$-A. Tight dimerization of the NBDs would then cause the TMDs to open at the periplasmic face for substrate entry (outward-facing conformation, as found e.g., for ATP-bound $MalFGK(E159Q)_2$-E). Next, hydrolysis of ATP directs the transition state back toward the resting state where the substrate is released on the cytoplasmic face of the membrane. The tweezers-like catalytic cycle of the NBDs was first proposed on the basis of the crystal structures of dimeric Rad50 and MalK (16,34). Binding of ATP to the (open) resting state of $MalK_2$ causes the dimer to close, thereby sandwiching the two ATPs between the interface of the N-terminal halves of the NBD. After hydrolysis of ATP and release of P_i, the dimer would then progress to the semiopen, ADP-bound state until it finally returns to the resting state after dissociation of ADP. MgATP-driven closure of the MalK-dimer has also been shown by a molecular dynamics simulation (35). After introduction of MgATP into the binding pockets, the authors could monitor a transition from the open to the semiopen or from the semiopen to the closed conformer. A spin-labeling study on conformational changes in the ABC-transporter MsbA was recently published by Borbat et al. (9). The authors could show large distance changes for several residues in the TM-domains and one residue in the NBDs of MsbA for the transition from the apo- to the vanadate-trapped state.

In this study, the combination of two methodologies such as SDSL EPR and site-directed chemical cross-linking is shown to be a valuable tool to obtain a detailed description at the molecular level of the $MalK_2$ rearrangements in the apo-, ATP-bound-, transition-, and posthydrolysis states. The EPR analysis was complemented by simulations carried out on in silico spin-labeled x-ray structures to predict the expected interspin distance constraints. The potentiality of this approach to validate the x-ray data and to model the structural changes starting from the available structure of a catalytic intermediate is shown as well.

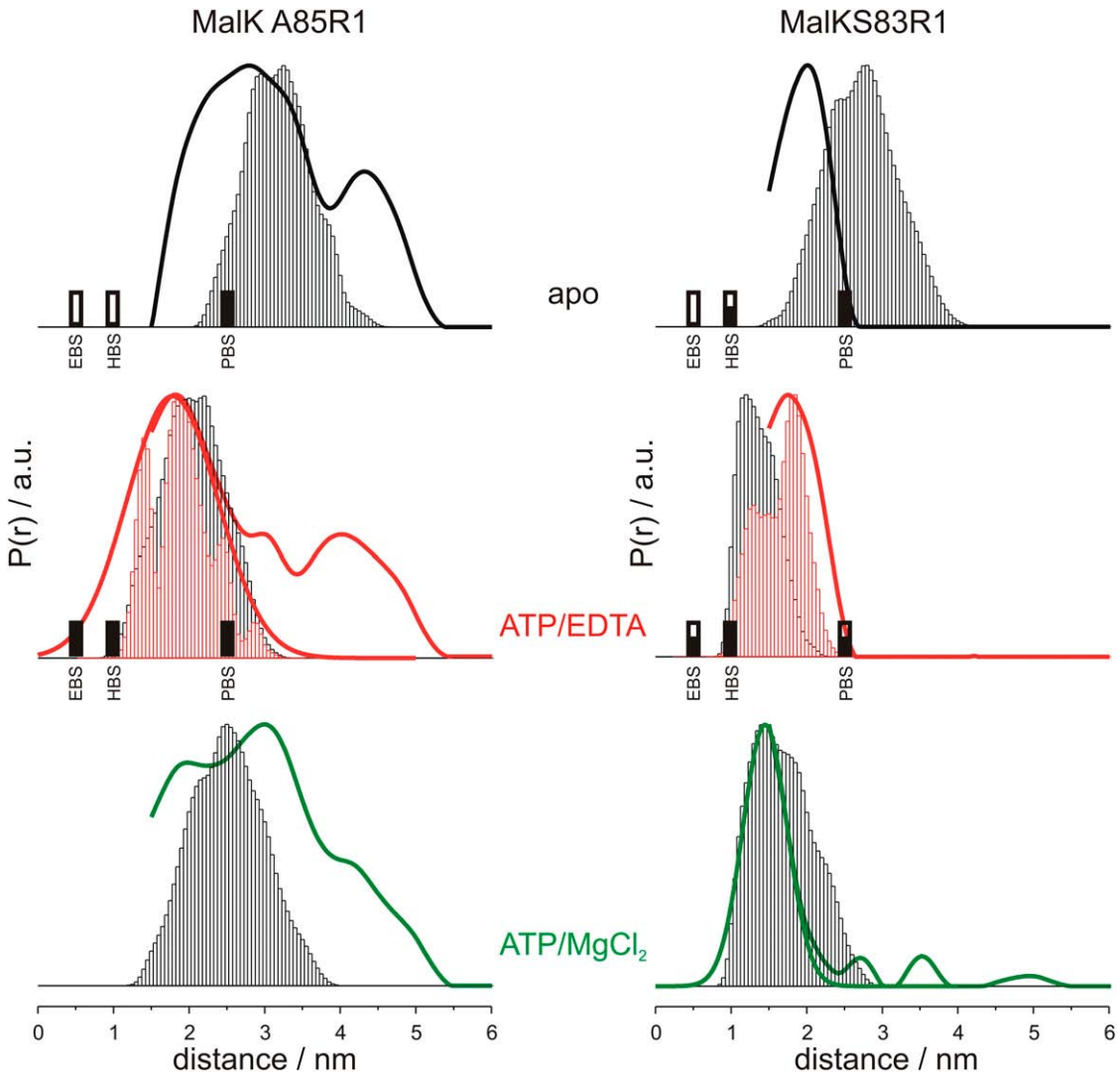

FIGURE 8 Comparison between experimental and simulated distance distributions for positions 83 and 85 in the apo-, ATP-bound-, and posthydrolysis-states. The EPR-derived data are represented as thick colored lines; the simulated distance distributions derived from spin-labeled isolated MalK domains are presented as black bar histograms superimposed to the EPR data. The simulated distribution derived from the labeled MalK assembled in the ATP-bound form of the complex is presented as red bar histogram and superimposed to the EPR data obtained for the ATP-bound state of the detergent solubilized complex. The amount of K-K dimer observed in the cross-linking studies for the three linkers (EBS, 0.5 nm; HBS, 1.0 nm; PBS, 2.5 nm) is also presented for the apo-, and ATP-bound states. Full black sticks positioned at the linker main distance represent the major product of the reaction; half full sticks indicate a certain degree of K-K dimer formation; empty sticks indicate that no K-K dimer is formed with that particular linker.

The presence of two native cysteines partially accessible to spin-labeling in the C-terminal (regulatory) subdomains of each MalK monomer allowed monitoring the overall rearrangement of this region of the NBDs on ATP binding. Due to the low labeling efficiency and the broad distance distribution obtained from the fit, these data can only be used as soft constraints in the analysis of the NBD motion during the catalytic cycle. The distance distribution was analyzed based on the Cβ-Cβ distances between the native cysteines (C352 and C362 in *E. coli* MalK) obtained from the x-ray structures of isolated and assembled MalK domains. The data suggest a small increase (<0.3 nm) mainly in the 350–360 and 350–360′ distances on ATP binding. This fact could be interpreted as a slight opening of the C-terminal domains in the ATP-bound state.

The interspin distance of 6 nm detected between positions 117 in the apo-state is in line with the long Cβ-Cβ distances measured in the crystal structure of the isolated $MalK_2$ (Table 1). The absence of significant changes between positions 117 in complex-assembled $MalK_2$ on ATP binding suggests a smaller rearrangement at the surface of the MalK dimer in the assembled than in the isolated form. The MalK dimer in the apo-state of the complex could be already more compact or different in terms of side chain dynamics.

The most dramatic distance changes were observed in the Q-loop (positions 83 and 85) by both cross-linking and EPR

(Fig. 8). The choice of two residues in close vicinity, however with different expected distance changes (Table 1), is of particular interest as it might help to differentiate the global rearrangements of the protein from the possible influences of the molecular micro-environment on the spin labels. The Q-loop, connecting the α-helical and the RecA-like subdomains of MalK, is in several respects important for the catalytic cycle of the transporter. First, it encompasses a conserved glutamine residue that binds to a Mg^{2+}-ion needed as a co-factor for ATP-hydrolysis. Second, it is involved in inter-domain signaling between NBDs and the TMDs (36–38). Genetic data (39), cross-linking experiments (17,19), and x-ray data on the assembled complex (6) suggest an interaction of the Q-loops with MalFG. Moreover, one of the unexpected features shown by the supercomplex structure is the insertion of the C-terminal tail of MalG into the MalK dimer interface. Residues 290–296 of MalG pack along the Q-loop (positions 83–89) of one MalK monomer, with the terminal carboxyl group of MalG making three hydrogen bonds with backbone atoms of the Q-loop in the opposing monomer (residues S83, A85, and L86). The coupling between the two MalK monomers by MalG seems to contribute to the ordering of the Q-loop and may be important in the formation of the catalytic intermediate conformation of the full transporter.

The cross-linking data obtained for the cysteines at positions 83 and 85 nicely correspond to the EPR findings for the same cysteines labeled with MTSSL. This comparison allows to rule out strong effects of label reorientation on the distance changes detected and to validate the interpretation of the interspin distance changes in terms of backbone rearrangements. The minor discrepancies observed could be explained by the different experimental strategies. Whereas EPR requires the permanent introduction of a spin label into the protein that might interfere with the structure as seen in the case of A85 (low activity), the determination of distances by cross-linking is highly influenced by side chain dynamics and molecular surrounding of the target residue. This might cause severe differences in reactivity for different sites in the protein. Furthermore, cross-linking possibly underestimates distances. Sun et al. (40) reported a similar situation for distances measured by EPR and cross-linking in Lac-permease of *E. coli*. They explain a possible underestimation of distances by cross-linking by the fact that even infrequent collisions between reactive pairs may lead to an accumulation of cross-linked product over time. This might be the reason why we see, for example, a K-K-dimer with a cross-linker like EBS (0.5 nm) in the vanadate-trapped state of S83C, where EPR analysis detected a mean distance of 1.6 nm (full width at half-maximum, 0.8 nm). Thus, we cannot claim that spin-labeling EPR does not impose any constraints on the experimental system and so would be closer to the unperturbed situation of the protein. However, the advantages of SDSL EPR can be seen in the fact that it permits a quantitative and more stringent analysis of the data that might in turn show some of the structural constraints imposed on the spin-labeled side chains.

Interestingly, the distance distribution obtained by EPR for A85R1 is characterized by the presence of several peaks, whereas a single well-defined distance distribution is found for S83R1 in all states investigated. We do not consider this as an artifact of sample preparation because the results were reproducible. Rather, we interpret this finding as being intrinsic to the very sensitive position of A85 in the architecture of the transporter. The crystal structure of $MalFGK(E159Q)_2$-E shows that hydrogen bonds are formed between G293 and G296 of MalG to the respective A85 residues of the two MalK-monomers. Whereas an exchange of A85 to cysteine does not have a severe effect on stability and activity of the complex, it caused a dramatic loss of stability for $MalK_2$ expressed as a soluble protein in the absence of MalFG (data not shown). Furthermore, attachment of MTSSL to position 85 in the complex leads to a rather drastic decrease of activity (20% residual activity, see above). Thus, the formation of potentially inactive protein species by labeling of this specific site might cause additional peaks in the distance distribution.

The distance between spin labels attached to position 85 decreases from 2.8 nm to 1.8 nm on ATP binding, with the transition state (vanadate-trapped state) closely resembling the ATP-bound state. Good correspondence was found between the experimentally determined peak maxima and the distance distribution resulting from the simulation carried out on in silico spin-labeled isolated $MalK_2$ crystal structures in the apo- and ATP-bound states (3.1 to 2.0 nm, see Fig. 8), thus supporting the notion of an open-to-close transition in the supercomplex similar to the one in the isolated NBDs. It is worth noting that, despite of a qualitative good agreement, the positions of the peak maxima obtained from the isolated MalK domains are slightly shifted with respect to the experimental distances measured in the assembled complex. On the other hand, an excellent agreement is found between simulated and experimental data in the ATP-bound form of the assembled complex.

In the posthydrolysis state, a reopening of $MalK_2$ at position 85 is detected, with the presence of two main peaks at 1.95 and 3 nm. The simulated distance distribution is centered at 2.5 nm. Again, the simulated peak maxima, despite being in qualitative agreement, do not perfectly coincide with the experimental data. This supports the notion of reopening of the NBDs in the complex similar to what is observed in the isolated NBDs with minor differences likely arising from the presence of TMDs.

On the contrary, the data for the spin-labeled position 83, located only two residues apart, are more difficult to correlate directly to this movement.

For all states investigated, the DEER distance distribution for S83R1 was very narrow and monomodal, which on the one hand makes this residue a good counterpart for a detailed structural study of the Q-loop. On the other hand, disentangling the influence of the spin-label side chain rotamers in a closely packed protein region from the backbone conformational changes strictly requires in silico spin-labeling and

analysis of the simulated distances. The experimentally obtained sharp distance distributions strongly suggest that position 83 is more involved than position 85 in tertiary interactions during all states of the nucleotide cycle in the assembled complex. This is probably due to the presence of MalG, modifying the overall interaction pattern.

Striking deviations between the simulated (isolated $MalK_2$) and experimental results are found especially in the apo-state where a broad distance distribution centered at 2.8 nm is simulated in the isolated domains whereas a narrow distance distribution centered at 2 nm is measured in the assembled complex. This indicates clearly that even in the absence of ATP the closely packed protein environment in the assembled complex leads to interspin distances shorter than expected in the isolated domains.

In the ATP-bound state, the simulation produced shorter distances in the isolated than in the assembled complex, the latter being in excellent agreement with the experimental results. In the posthydrolysis state, the simulations carried out on isolated domains better represent the EPR data, even though the experimental distance distribution is somewhat narrower and its mean value is shifted to shorter distances.

The good correspondence found between the experimentally determined peak maxima and the distances resulting from in silico spin-labeling of the isolated $MalK_2$ crystal structures for position 85 support the notion of an open-to-close transition in the assembled complex similar to the one in the isolated NBDs. However, strong indications exist from the analysis of position 83 that the presence of MalG might modify the overall interaction pattern, especially in the apo-state. Based on these results, the apo-state of the isolated NBDs obtained by x-ray crystallography is clearly not representative for the assembled NBDs.

CONCLUSIONS AND OUTLOOK

In this study, we presented a site-directed spin-labeling approach aimed to determine interside chain distances on spin-labeled mutants of the maltose-ABC-importer, in combination with site-directed chemical cross-linking and a fast interspin distances simulation method based on spin label rotamer libraries. The data obtained allowed us to accurately monitor molecular rearrangements in the nucleotide-binding subunits of purified $MalFGK_2$ in detergent solution.

In summary, we have provided a fine-grained analysis of distance changes for three engineered and two native cysteine sites in the MalK subunits of the assembled transporter at individual steps of the transport cycle. The C-terminal domains of $MalK_2$ undergo only a slight rearrangement (<0.3 nm) in the ATP-bound state. Concomitantly, the outer surfaces of the N-terminal domains do not move closer on ATP binding. On the contrary, the Q-loop undergoes the most dramatic distance changes during the catalytic cycle. Positions 85 come close together in the ATP-bound state and in the vanadate-trapped intermediate and move back toward the apo-state after ATP hydrolysis. The distance between positions 83 is shown to slightly decrease on ATP binding, and to further decrease after ATP hydrolysis. We found significant deviations especially in the apo- and, to a minor extent, in the posthydrolysis states between the experimental results and the simulations based on isolated $MalK_2$, especially for position 83. This fact points to potentially functionally relevant interactions of this side chain with the transmembrane components, most probably with the C-terminal tail of MalG. Based on EPR and chemical cross-linking data and supported by in silico analyses, we propose a slightly modified version of the tweezers-like motion of the NBDs in the transport complex, in which the apo-state of the NBDs is more compact, likely due to interactions with MalG.

Molecular modeling based on the assembled complex structure in combination with the EPR distance constraints and the available data on the isolated domain rearrangements during the catalytic cycle would help to monitor at a molecular level the motional changes of the NBDs in the assembled transporter. Clearly, it is now tempting to probe this model by taking snapshot pictures for all steps of the transport process with the EPR/cross-linking experimental system established for the maltose transporter. Studies addressing the interdomain communication between NBD domains and key residues in MalF, MalG, and MalE are in progress in our laboratories.

M.G. and E.S. thank Dr. Peter Müller and Prof. Andreas Herrmann (Molecular Biophysics, Humboldt Universität zu Berlin) for their contributions to an earlier state of the project and Heidi Landmesser (Humboldt Universität zu Berlin) for excellent technical assistance. E.B. thanks D. Wunnicke for in silico spin-labeling of positions 117 in the MalK subunits. Figs. 1 and 7 were created with VMD and rendered with POV-ray.

This work was supported by Deutsche Forschungsgemeinschaft grant SCHN 274/9-3 (E.S.), by a fellowship of the German National Academic Foundation (M.G.), by the VolkswagenStiftung grant I-80842 (E.B. and H.-J.S.), by Deutsche Forschungsgemeinschaft grant STE 640/7-2 (H.-J.S.), and by Deutsche Forschungsgemeinschaft grant JE 246/3-2 (G.J.).

REFERENCES

1. Holland, I. B., S. Cole, K. Kuchler, and C. F. Higgins, editors. 2003. ABC Proteins: From Bacteria to Man. Academic Press, New York.
2. Dassa, E. 2003. Phylogenetic and functional classification of ABC (ATP-binding cassette) systems. *In* ABC Proteins: From Bacteria to Man. I. B. Holland, S. Cole, K. Kuchler, and C. F. Higgins, editors. Academic Press, New York. 3–35.
3. Dawson, R. J. P., and K. P. Locher. 2006. Structure of a bacterial multidrug ABC transporter. *Nature*. 443:180–185.
4. Hvorup, R. N., B. A. Goetz, M. Niederer, K. Hollenstein, E. Perozo, and K. P. Locher. 2007. Asymmetry in the structure of the ABC transporter-binding protein complex BtuCD-BtuF. *Science*. 317:1387–1390.
5. Hollenstein, K., D. C. Frei, and K. P. Locher. 2007. Structure of an ABC transporter in complex with its binding protein. *Nature*. 446:213–216.
6. Oldham, M. L., D. Khare, F. A. Quiocho, A. L. Davidson, and J. Chen. 2007. Crystal structure of a catalytic intermediate of the maltose transporter. *Nature*. 450:515–522.
7. Bordignon, E., and H. J. Steinhoff. 2007. Membrane protein structure and dynamics studied by site-directed spin-labeling ESR. *In* ESR

Spectroscopy in Membrane Biophysics. M. A. Hemminga and L. J. Berliner, editors. Springer, New York. 129–164.

8. Jeschke, G., C. Wegener, M. Nietschke, H. Jung, and H. J. Steinhoff. 2004. Interresidual distance determination by four-pulse double electron-electron resonance in an integral membrane protein: the Na^+/proline transporter PutP of *Escherichia coli*. *Biophys. J.* 86:2551–2557.
9. Borbat, P. P., K. Surendhran, M. Bortolus, P. Zou, J. H. Freed, and H. S. McHaourab. 2007. Conformational motion of the ABC transporter MsbA induced by ATP hydrolysis. *PLoS Biol.* 5:e271.
10. Smirnova, I., V. Kasho, J.-Y. Choe, C. Altenbach, W. L. Hubbell, and H. R. Kaback. 2007. Sugar binding induces an outward facing conformation of LacY. *Proc. Natl. Acad. Sci. USA.* 104:16504–16509.
11. Schneider, E. 2003. Import of solutes by ABC-transporters—the maltose and other systems. *In* ABC Proteins: From Bacteria to Man. I. B. Holland, S. Cole, K. Kuchler, and C. F. Higgins, editors. Academic Press, New York. 157–185.
12. Davidson, A. L., and J. Chen. 2004. ATP-binding cassette transporters in bacteria. *Annu. Rev. Biochem.* 73:241–268.
13. Lu, G., J. M. Westbrooks, A. L. Davidson, and J. Chen. 2005. ATP hydrolysis is required to reset the ATP-binding cassette dimer into the resting-state conformation. *Proc. Natl. Acad. Sci. USA.* 102:17969–17974.
14. Daus, M. L., H. Landmesser, A. Schlosser, P. Muller, A. Herrmann, and E. Schneider. 2006. ATP induces conformational changes of periplasmic loop regions of the maltose ATP-binding cassette transporter. *J. Biol. Chem.* 281:3856–3865.
15. Schneider, E., and S. Hunke. 1998. ATP-binding-cassette (ABC) transport systems: functional and structural aspects of the ATP-hydrolyzing subunits/domains. *FEMS Microbiol. Rev.* 22:1–20.
16. Chen, J., G. Lu, J. Lin, A. L. Davidson, and F. A. Quiocho. 2003. A tweezers-like motion of the ATP-binding cassette dimer in an ABC transport cycle. *Mol. Cell.* 12:651–661.
17. Daus, M. L., M. Grote, P. Muller, M. Doebber, A. Herrmann, H. J. Steinhoff, E. Dassa, and E. Schneider. 2007. ATP-driven MalK dimer closure and reopening and conformational changes of the ''EAA'' motifs are crucial for function of the maltose ATP-binding cassette transporter ($MalFGK_2$). *J. Biol. Chem.* 282:22387–22396.
18. Jones, P. M., and A. M. George. 2004. The ABC transporter structure and mechanism: perspectives on recent research. *Cell. Mol. Life Sci.* 61:682–699.
19. Hunke, S., M. Mourez, M. Jehanno, E. Dassa, and E. Schneider. 2000. ATP modulates subunit-subunit interactions in an ATP-binding cassette transporter ($MalFGK_2$) determined by site-directed chemical cross-linking. *J. Biol. Chem.* 275:15526–15534.
20. Landmesser, H., A. Stein, B. Bluschke, M. Brinkmann, S. Hunke, and E. Schneider. 2002. Large-scale purification, dissociation and functional reassembly of the maltose ATP-binding cassette transporter ($MalFGK_2$) of *Salmonella typhimurium*. *Biochim. Biophys. Acta.* 1565:64–72.
21. Daus, M. L., S. Berendt, S. Wuttge, and E. Schneider. 2007. Maltose binding protein (MalE) interacts with periplasmic loops P2 and P1 respectively of the MalFG subunits of the maltose ATP binding cassette transporter ($MalFGK_2$) from *Escherichia coli*/*Salmonella* during the transport cycle. *Mol. Microbiol.* 66:1107–1122.
22. Loo, T. W., and D. M. Clarke. 2001. Determining the dimensions of the drug-binding domain of human P-glycoprotein using thiol cross-linking compounds as molecular rulers. *J. Biol. Chem.* 276:36877–36880.
23. Steinhoff, H. J., N. Radzwill, W. Thevis, V. Lenz, D. Brandenburg, A. Antson, G. Dodson, and A. Wollmer. 1997. Determination of interspin distances between spin labels attached to insulin: Comparison of electron paramagnetic resonance data with the x-ray structure. *Biophys. J.* 73:3287–3298.
24. Steinhoff, H. J., A. Savitsky, C. Wegener, M. Pfeiffer, M. Plato, and K. Möbius. 2000. High-field EPR studies of the structure and conformational changes of site-directed spin-labeled bacteriorhodopsin. *Biochim. Biophys. Acta.* 1457:253–262.
25. Plato, M., H. J. Steinhoff, C. Wegener, J. T. Törring, A. Savitsky, and K. Möbius. 2002. Molecular orbital study of polarity and hydrogen bonding effects on the g and hyperfine tensors of site directed NO spin labeled bacteriorhodopsin. *Mol. Phys.* 100:3711–3721.
26. Brutlach, H., E. Bordignon, L. Urban, J. P. Klare, H.-J. Reyer, M. Engelhard, and H. J. Steinhoff. 2006. High-field EPR and site directed spin labeling reveal a periodical polarity profile: the sequence 88–94 of the photo transducer NpHtrII in complex with sensory rhodopsin, NpSRII. *Appl. Magn. Reson.* 30:359–372.
27. Pannier, M., S. Veit, A. Godt, G. Jeschke, and H. W. Spiess. 2000. Dead-time free measurement of dipole-dipole interactions between electron spins. *J. Magn. Reson.* 142:331–340.
28. Jeschke, G., V. Chechik, P. Ionita, A. Godt, H. Zimmermann, J. Banham, C. R. Timmel, D. Hilger, and H. Jung. 2006. DeerAnalysis2006—a comprehensive software package for analyzing pulsed ELDOR data. *Appl. Magn. Reson.* 30:473–498.
29. Jeschke, G., and Y. Polyhach. 2007. Distance measurements on spin-labeled biomacromolecules by pulsed electron paramagnetic resonance. *Phys. Chem. Chem. Phys.* 9:1895–1910.
30. Dulley, J. R., and P. A. Grieve. 1975. Simple technique for eliminating interference by detergents in Lowry method of protein determination. *Anal. Biochem.* 64:136–141.
31. Maryasov, A. G., and Y. D. Tsvetkov. 2000. Formation of the pulsed-electron double resonance signal in the case of a finite amplitude of microwave fields. *Appl. Magn. Reson.* 18:583–605.
32. Bode, B. E., D. Margraf, J. Plackmeyer, G. Durner, T. F. Prisner, and O. Schiemann. 2007. Counting the monomers in nanometer-sized oligomers by pulsed electron-electron double resonance. *J. Am. Chem. Soc.* 129:6736–6745.
33. Hollenstein, K., R. J. P. Dawson, and K. P. Locher. 2007. Structure and mechanism of ABC transporter proteins. *Curr. Opin. Struct. Biol.* 17:412–418.
34. Hopfner, K. P., A. Karcher, D. S. Shin, L. Craig, L. M. Arthur, J. P. Carney, and J. A. Tainer. 2000. Structural biology of Rad50 ATPase: ATP-driven conformational control in DNA double-strand break repair and the ABC-ATPase superfamily. *Cell.* 101:789–800.
35. Oloo, E. O., E. Y. Fung, and D. P. Tieleman. 2006. The dynamics of the MgATP-driven closure of MalK, the energy-transducing subunit of the maltose ABC transporter. *J. Biol. Chem.* 281:28397–28407.
36. Loo, T. W., M. C. Bartlett, and D. M. Clarke. 2002. The ''LSGGQ'' motif in each nucleotide-binding domain of human P-glycoprotein is adjacent to the opposing Walker A sequence. *J. Biol. Chem.* 277: 41303–41306.
37. Urbatsch, I. L., K. Gimi, S. Wilke-Mounts, and A. E. Senior. 2000. Investigation of the role of glutamine-471 and glutamine-1114 in the two catalytic sites of P-glycoprotein. *Biochemistry.* 39:11921–11927.
38. Dalmas, O., C. Orelle, A. E. Foucher, C. Geourjon, S. Crouzy, A. Di Pietro, and J. M. Jault. 2005. The Q-loop disengages from the first intracellular loop during the catalytic cycle of the multidrug ABC transporter BmrA. *J. Biol. Chem.* 280:36857–36864.
39. Mourez, M., N. Hofnung, and E. Dassa. 1997. Subunit interactions in ABC transporters: a conserved sequence in hydrophobic membrane proteins of periplasmic permeases defines an important site of interaction with the ATPase subunits. *EMBO J.* 16:3066–3077.
40. Sun, J. Z., J. Voss, W. L. Hubbell, and H. R. Kaback. 1999. Proximity between periplasmic loops in the lactose permease of *Escherichia coli* as determined by site-directed spin labeling. *Biochemistry.* 38:3100–3105.